remote sensing

MDPI

Article

The Performance of GPM IMERG Product Validated on Hourly Observations over Land Areas of Northern Hemisphere

Pengfei Lv and Guocan Wu *

State Key Laboratory of Earth Surface Processes and Resource Ecology, Faculty of Geographical Science, Beijing Normal University, Beijing 100875, China; 202121490034@mail.bnu.edu.cn
* Correspondence: gcwu@bnu.edu.cn

Abstract: The integrated multi-satellite retrievals for the global precipitation measurement (IMERG) data, which is the latest generation of multi-satellite fusion inversion precipitation product provided by the Global Precipitation Measurement (GPM) mission, has been widely applied in hydrological research and applications. However, the quality of IMERG data needs to be validated, as this technology is essentially an indirect way to obtain precipitation information. This study evaluated the performance of IMERG final run (version 6.0) products from 2001 to 2020, using three sets of gauge-derived precipitation data obtained from the Integrated Surface Database, China Meteorological Administration, and U.S. Climate Reference Network. The results showed a basic consistency in the spatial pattern of annual precipitation total between IMERG data and gauge observations. The highest and lowest correlations between IMERG data and gauge observations were obtained in North Asia (0.373, $p < 0.05$) and Europe (0.308, $p < 0.05$), respectively. IMERG data could capture the bimodal structure of diurnal precipitation in South Asia but overestimates a small variation in North Asia. The disparity was attributed to the frequency overestimation but intensity underestimation in satellite inversion, since small raindrops may evaporate before arriving at the ground but can be identified by remote sensors. IMERG data also showed similar patterns of interannual precipitation variability to gauge observation, while overestimating the proportion of annual precipitation hours by 2.5% in North America, and 2.0% in North Asia. These findings deepen our understanding of the capabilities of the IMERG product to estimate precipitation at the hourly scale, and can be further applied to improve satellite precipitation retrieval.

Keywords: IMERG; spatial pattern; error analysis; diurnal variation; interannual variability

Citation: Lv, P.; Wu, G. The Performance of GPM IMERG Product Validated on Hourly Observations over Land Areas of Northern Hemisphere. *Remote Sens.* **2024**, *16*, 4334. https://doi.org/10.3390/rs16224334

Academic Editor: Marios Anagnostou

Received: 29 September 2024
Revised: 5 November 2024
Accepted: 16 November 2024
Published: 20 November 2024

1. Introduction

Precipitation is a key variable in regional hydrology research, and is quite susceptible to climate change. Therefore, precipitation data with high quality is greatly important for hydrological research and applications, which mainly come from satellite inversion for the spatiotemporal continuity. Along with the development and application of remote sensing technology, the inversion of satellite-derived precipitation data plays an increasingly important role in fields such as meteorological monitoring, water resource management, and environmental protection [1–5]. Satellite products can provide precipitation estimates with high spatiotemporal resolution owing to their advanced algorithms and plentiful sensors and have broad application prospects [6–8]. However, there are still some concerns in regard to the accuracy and reliability of precipitation data derived from satellites, as this technology is essentially an indirect way to obtain precipitation information [1,9,10]. Therefore, many satellite products have been subjected to comprehensive and detailed quality assessments to verify their accuracy in estimating different precipitation indicators [11–14].

Considering that precipitation data obtained from meteorological stations are regarded as the most representative of reality, validation based on station-derived observations has become one of the key methods for evaluating the performance of satellite products [9,11,15].

The accuracy of satellite data at different temporal and spatial scales can be directly verified via comparisons with observations obtained from meteorological stations [12,15–17]. Existing research has shown that daily satellite-derived data are quite consistent with daily precipitation observations at the regional scale [18–20]. However, satellite products may not provide reliable estimates in areas with complex terrain, such as mountains and plateaus [5,21,22]. For example, assessments conducted based on station-derived observations in high-altitude regions of Asia have shown that the precipitation from satellite products was closer to observations than reanalysis products, but the former technology still had difficulties in capturing solid precipitation in winter [23].

Due to the various sensors installed on different satellites and the remote sensing inversion algorithms used, this technology widely varies in terms of its capability to characterize precipitation in different regions [24–26]. Previous studies have found that the performance of precipitation products varies greatly at different temporal and spatial scales, with the assessments of different products in the same region possibly showing significantly different results [27,28]. Accuracy tests evaluating inversion in multiple products have revealed that almost all of them had poor inversion capabilities under weak and extremely strong precipitation in warm regions [29]. When estimating precipitation on different surfaces or at different frequencies, the systematic deviation of satellite products on land is much smaller than that over the ocean. These products are more likely to produce positive deviations under low rainfall intensity and negative deviations under high rainfall intensity on land, while generally producing negative deviations for all precipitation intensities over the ocean [26].

Current assessments of satellite precipitation products mainly consider daily time scales. The seasonal accuracy of satellite-derived precipitation estimates for tropical rainfall measuring mission has been evaluated relative to ground precipitation data using statistical methods [30]. Precipitation data obtained from six satellite products with a high spatiotemporal resolution were evaluated in the sub-Saharan region at three time scales (i.e., daily, monthly, and yearly) as well as at two spatial scales (i.e., pixel and watershed) using different quantitative and qualitative statistical indicators. The results showed that satellite products could provide precipitation estimates that were close to station observations at all three temporal scales, potentially making them a valuable alternative to rain gauges [31]. An evaluation of light rainfall data obtained from satellite products at the daily scale in the Chinese mainland also demonstrated the successful detection of the spatial pattern of light rainfall, although the detection ability for small rainfall events (less than 5 mm/d) was limited. In areas characterized by more complex winter precipitation types, satellite products generally perform poorly, showing a relatively large deviation in the estimation of light rainfall [32].

Along with the development of remote sensing technology and the advancement of inversion algorithms, more and more precipitation products with a high spatiotemporal resolution have been released to the public. The integrated multi-satellite retrievals for the global precipitation measurement (GPM) product (hereafter referred to as IMERG) has received significant attention in recent years as it represents a new generation of global satellite precipitation products [33]. Numerous studies have evaluated the accuracy of IMERG data in recent years [17,34–36]. IMERG has a higher spatiotemporal resolution and provides significantly more accurate precipitation estimates compared with products of the previous generation, and it also has broader application prospects in various research fields [17,26,35,37–39]. When considering the estimation of extreme precipitation, the performance of IMERG is relatively consistent with that of its predecessors in terms of precipitation distribution, but the new technology has significant advantages in the estimation of heavy precipitation [37]. IMERG has also demonstrated a greatly improved ability to detect rainfall in the high altitude areas, such as southern region of the Tibetan Plateau [39].

The evaluations of satellite precipitation products primarily aim to reveal their error sources and improve the inversion algorithms. Although such observations at the monthly

scale were used to correct IMERG and improve its ability to measure precipitation, inversion uncertainties at higher temporal resolutions are still present due to diverse land surfaces and climate conditions. The study of diurnal cycle also requires high temporal precipitation data, such as hourly scale, which is a fundamental cycle in the Earth system and related to both regional and large-scale thermodynamic processes [21,40,41]. Therefore, quality assessments are necessary before using IMERG-derived hourly data for hydrological and meteorological research. Currently, IMERG data are generally evaluated at the regional or continental scale [34,42–44], but few studies have also accessed their accuracy globally due to the sparse spatiotemporal distribution of station-derived observations that can be used as a test bed [26]. It is found that GPM IMERG performs better than other satellite products in reproducing spatiotemporal patterns and variability of extreme precipitation [35]. Attributing to gauge adjustment, the systematic differences over land in IMERG data are much smaller compared to those over ocean [26], but the precipitation amount and frequency ratios in the IMERG data are usually overestimated [34].

This study aimed to comprehensively evaluate IMERG data using hourly gauge observations collected from several meteorological institutions. The meteorological stations were distributed over the main land areas including North America, Europe and Asia, and the study period involved the latest two decades (2001–2020). Specifically, the proportion of precipitation hours and hourly precipitation intensity were compared between IMERG data and meteorological observations. The regional differences between the two datasets were compared and analyzed based on several error indicators. The ability of IMERG data to accurately reflect the diurnal cycle and interannual variability of hourly precipitation was also evaluated. The results can contribute to our understanding of satellite precipitation retrieval in climate change and hydrological monitoring.

2. Materials and Methods

2.1. Precipitation Data

2.1.1. Integrated Surface Database

The Integrated Surface Database (ISD) is a global dataset comprising hourly and synoptic surface observations compiled from numerous sources. It integrates data from more than 100 original sources and includes numerous data formats derived from many early precipitation records. This dataset is currently one of the largest in the world in terms of total data volume; it has also the highest station density and fastest data update frequency, and is equipped with a quality control module to ensure data integrity and accuracy [45].

2.1.2. Hourly Precipitation Observations from National Surface Stations in China

The surface stations distributed across China and collecting precipitation information are one of the most important data sources for studying climate and environmental changes in China [4,46–48]. These data, which are managed by the China Meteorological Administration (CMA), are recorded from stations located in different geographical environments, including cities, rural areas, mountainous areas, and plains. The observation equipment undergoes regular calibration and maintenance to ensure the reliability and accuracy of the collected data. Precipitation observations are collected hourly from 2420 national meteorological stations, and their accuracy is ensured through the quality control and consistency testing [49,50].

2.1.3. U.S. Climate Reference Network

The U.S. Climate Reference Network (USCRN) is a systematic and sustained network of climate monitoring stations distributed across the contiguous U.S., Alaska, and Hawaii. It has provided high-quality measurements of precipitation and other climate variables at about 225 sites since the year 2000, to monitor climate change and its impacts [51]. These stations are distributed to ensure that all major nodes of regional climate variability are captured while taking into account large scale regional topographic factors. Advanced

instruments are equipped to continuously provide hourly observations with accuracy and reliability, by improving the measurement accuracy, sensor stability, and the optimization of data processing algorithms. These improvements enable the network to play an important role in monitoring precipitation trends as well as providing reliable data support for climate research, water resource management, and weather warning [51]. The USCRN stations are widely distributed across various geographical regions, including mountainous areas, plains, and coastal areas. Therefore, they can monitor a wide range of local climate conditions and trends, considering the influence of geographical characteristics, climate types, and population distribution.

2.1.4. IMERG Precipitation Data

The GPM IMERG product represents a new generation of global satellite precipitation products released in recent years [33]. Being equipped with an advanced dual-frequency precipitation radar and using improved algorithms, it has a higher accuracy, wider coverage range, and higher spatiotemporal resolution than its predecessors. Rainfall and snowfall data on a global scale are provided every 30 min based on microwaves within 3 h and the IMERG algorithm, and they can be used to promote research and applications in disciplines such as hydrology, meteorology, agriculture, disaster management [19,52–54].

The IMERG product has a spatial resolution of $0.1^\circ \times 0.1^\circ$ and a temporal resolution of 0.5 h. To meet the needs of different users, three IMERG product types have been developed, i.e., near real-time "Early-run" (IMERG_E), "Late-run" (IMERG_L), and post real-time "Final-run" (IMERG_F), releasing data with delays of 4 h, 14 h, and 3 months, respectively [33]. To reduce product bias, climate-related adjustments are made in IMERG_E and IMERG_L, while adjustments related to monthly precipitation observations are made in IMERG_F. Various versions of these IMERG products have been developed and the technology has been continuously improved [55]. In this study, data obtained from IMERG-F V6 covering the period from January 2001 to December 2020 and the region between 60°N and 60°S were selected for analysis.

2.2. Methods of Analysis

2.2.1. Data Processing

To be consistent with the time span of IMERG precipitation data, hourly precipitation observations from the ISD, CMA, and USCRN datasets between 2001 and 2020 were selected as validation data. To assess IMERG data quality across different global regions, the precipitation amounts from previous hour to the current hour recorded in Coordinated Universal Time (UTC) were chosen as the observations at this hour. Due to the maintenance of equipment at meteorological stations as well as their spatial distribution and relocation across different regions, a proportion of effective observations throughout the year of no less than 90% was required to ensure data consistency and reduce sampling errors. The IMERG product with a temporal resolution of 0.5 h was added for the hourly retrieval of precipitation data.

Because the precipitation observations were collected at meteorological stations, and the IMERG products were available at the $0.1^\circ \times 0.1^\circ$ grid, the gauge observation datasets (i.e., ISD, CMA, and USCRN) were matched with the grid in GPM IMERG based on the station location to avoid the errors introduced by any interpolation. Specifically, if only one station fell into a given $0.1^\circ \times 0.1^\circ$ grid, the precipitation records from that station were compared with those from the IMERG grid. If a grid contained two or more stations, the average precipitation metrics obtained from all stations within the grid was used as the observation for that grid [12,47]. The spatial range of IMERG data considered in this study was between 60°N and 60°S, and stations beyond these latitudes were not included. A regional analysis among different continents was conducted based on previous studies, as shown in Figure 1 [52,56]. Due to the limited availability of ground station data, the analysis focused on regions with a relatively large number of stations for validation, specifically

North America, Europe, North Asia, and South Asia, which have 223, 152, 1786 and 999 stations, respectively.

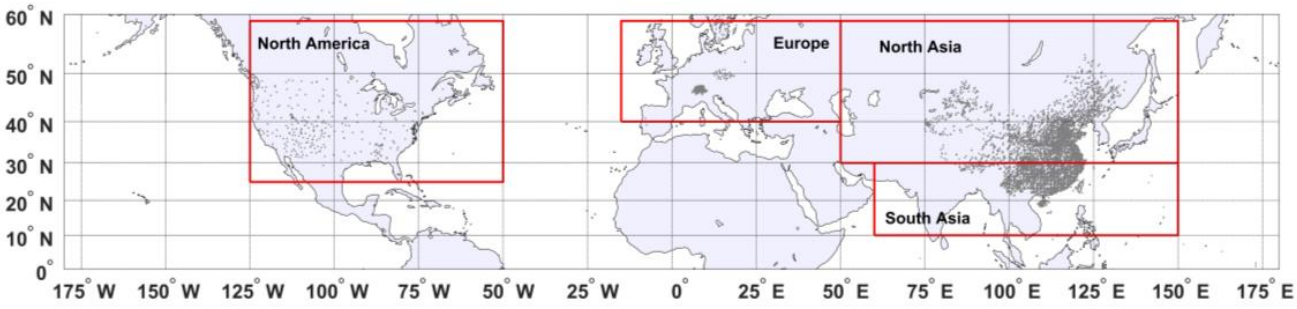

Figure 1. Spatial distribution of meteorological stations used in this study over land areas of the northern hemisphere. The four rectangles represent the regions with a relatively large number of stations: North America (25°–59°N, 125°–50°W), Europe (40°–59°N, 15°W–50°E), North Asia (30°–59°N, 50°–150°E), and South Asia (10°–30°N, 60°–150°E).

2.2.2. Statistical Indicators

To analyze the capability of IMERG to estimate precipitation, the following three parameters were considered: annual precipitation total, annual precipitation frequency, and precipitation intensity. Annual precipitation total is the sum of all hourly precipitation amounts throughout the year and is measured in mm/y; annual precipitation frequency is the number of records greater than 0.1 mm/h divided by the total number of hours throughout the year and is expressed as a percentage; and finally, precipitation intensity is the annual precipitation total divided by the number of hours with records greater than 0.1 mm/h throughout the year. The spatial differences in the multi-year averages of these parameters between station-derived observations and IMERG data were analyzed and compared.

The ability of IMERG to estimate precipitation at the hourly time scale was evaluated by comparing its estimates with observations derived from meteorological stations using conventional statistical indicators [57,58], including the Pearson correlation coefficient (CC), Mean Absolute Error (MAE), Root Mean Square Error (RMSE), and Relative Bias (RB). CC reveals the linear relationship between satellite-derived precipitation data and station observations; the closer the CC value is to 1, the stronger the correlation. Additionally, the one-sample *t*-test at 0.05 level is used to detect whether the generated correlation coefficient is significant. MAE represents the average of the absolute differences between the two types of data. RMSE measures the degree of dispersion between the two datasets; the closer the RMSE value is to 0, the smaller the degree of dispersion. RB indicates the percentage of the difference between satellite-derived precipitation data and station observations relative to the latter; the smaller the bias is, the closer the error is to 0.

The diurnal variation of the gauge-derived and IMERG data can be illustrated by the changes of hourly total precipitation, frequency, and intensity throughout the day (24 h). Several qualitative indicators are commonly used to measure the capabilities of satellite precipitation products. Similar to previous studies, the data obtained from IMERG at different hours of the day were evaluated using the following metrics [10,21,47,59]: Probability of Detection (POD), False Alarm Ratio (FAR), and Critical Success Index (CSI). Specifically, POD represents the fraction of precipitation hours that IMERG detects among the total actual precipitation hours, and FAR represents the fraction of unreal precipitation hours among all the hours recorded by IMERG [60]. The CSI can actually be expressed as a function of POD and FAR combining the characteristics of false alarms and missed precipitation hours [61]. These metrics comprehensively assess the performance of satellite precipitation products, clearly determining their advantages and disadvantages [15,18]. The methods used to calculate these parameters and their optimal values are shown in Table 1.

Table 1. Equations used to calculate the metrics for the evaluation of IMERG precipitation data and their optimal values. In these formulas, N represents the number of samples, S_n and σ_S represent satellite-derived precipitation data and standard deviation, respectively, while G_n and σ_G represent gauge observations and standard deviation, respectively. Additionally, n_{11} denotes the number of hours for which both gauge observations and IMERG precipitation data were obtained, n_{10} represents the hours for which IMERG data were obtained but gauge observations were not, n_{01} denotes the opposite of n_{10}, and n_{00} represents the hours for which neither records were obtained.

Metric	Formula	Optimal Value	Reference
Correlation Coefficient	$CC = \frac{\frac{1}{N}\sum_{n=1}^{N}(S_n - \overline{S})(G_n - \overline{G})}{\sigma_S \sigma_G}$	1	Yong et al., 2010 [57]
Mean Absolute Error	$MAE = \frac{1}{N}\sum_{n=1}^{N}\lvert S_n - G_n \rvert$	0	Yong et al., 2010 [57]
Root Mean Square Error	$RMSE = \sqrt{\frac{1}{N}\sum_{n=1}^{N}(S_n - G_n)^2}$	0	Yong et al., 2010 [57]
Relative Bias	$RB = \frac{\frac{1}{N}\sum_{n=1}^{N}(S_n - G_n)}{\frac{1}{N}\sum_{n=1}^{N} G_n} \times 100\%$	0	Yong et al., 2010 [57]
Probability of Detection	$POD = \frac{n_{11}}{n_{11} + n_{01}}$	1	Ebert et al., 2007 [60]
False Alarm Ratio	$FAR = \frac{n_{10}}{n_{11} + n_{10}}$	0	Ebert et al., 2007 [60]
Critical Success Index	$CSI = \frac{n_{11}}{n_{11} + n_{01} + n_{10}}$	1	Gerapetritis and Pelissier, 2004 [61]

3. Results

3.1. Spatial Patterns of IMERG Precipitation Data and Gauge Observations

As shown in Figure 2(a1–d1, a2–d2), the annual precipitation total records obtained from IMERG and meteorological stations exhibited a very similar spatial pattern, although IMERG generally overestimated this parameter. The relative bias of IMERG data with respect to gauge observation was also calculated, and the regional mean RB statistics are reported in Table 2. The IMERG precipitation data obtained for China largely reflected the spatial patterns of gauge observations, and specifically the spatial distribution divided by the Qinling-Huaihe Line. The southeastern coastal region of China was characterized by abundant precipitation, with annual totals exceeding 800 mm/y, and even reaching up to 2000 mm/y in some areas. Precipitation decreased progressively from the southeast to the northwest. Specifically, the northwestern inland regions experienced sparse precipitation

with annual totals below 800 mm/y, while in most of the other areas total precipitation reached less than 400 mm/y annually.

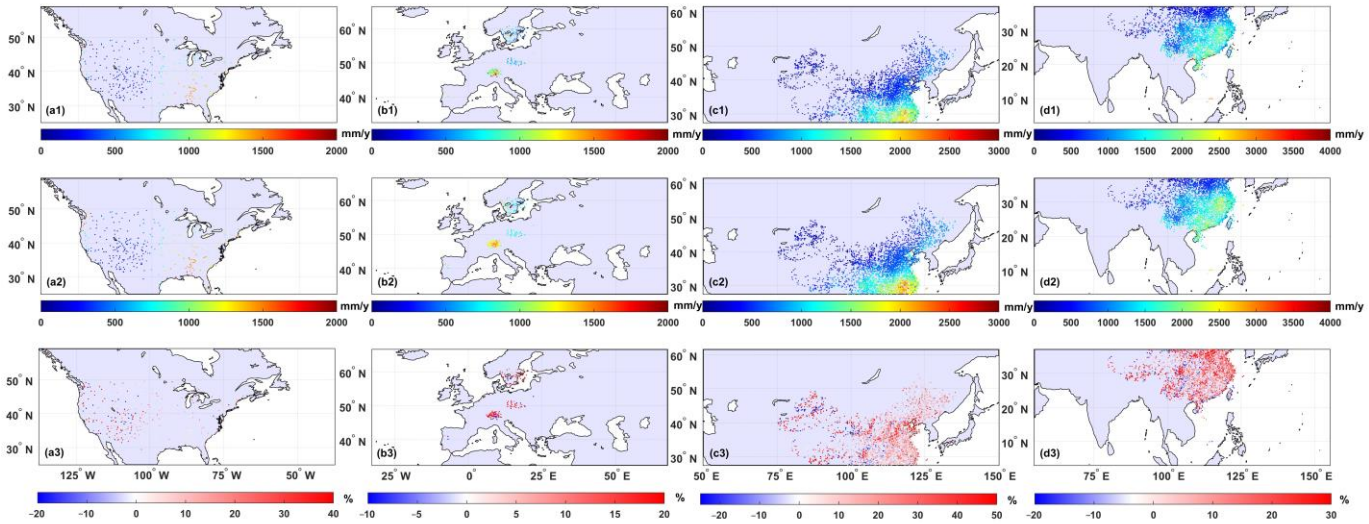

Figure 2. Average annual precipitation total from 2001 to 2020 obtained from gauge observations (**a1**–**d1**) and IMERG data (**a2**–**d2**), and the bias of IMERG data relative to gauge observations (**a3**–**d3**), for North America, Europe, North Asia, and South Asia, respectively.

Table 2. Variability of hourly precipitation in different regions as revealed by the Pearson Correlation Coefficient (CC), Mean Absolute Error (MAE), Root Mean Square Error (RMSE), Relative Bias (RB), Probability of Detection (POD), False Alarm Ratio (FAR), and Critical Success Index (CSI). "*" denotes statistical significance at the 0.05 level.

	North America	Europe	North Asia	South Asia
CC	0.367 *	0.308 *	0.373 *	0.350 *
MAE (mm/h)	0.131	0.155	0.115	0.223
RMSE (mm/h)	0.880	0.761	0.842	1.291
RB	22.7%	27.7%	28.0%	12.7%
POD	49.2%	41.9%	51.0%	49.3%
FAR	69.6%	54.8%	62.6%	55.1%
CSI	22.7%	27.4%	27.2%	30.1%

In North America, the special distributions of both IMERG data and gauge observations were also quite similar. To the west of 100°W, both methods recorded annual precipitation totals below 800 mm/y, with most areas reaching around 400 mm/y. In the Pacific Northwest, due to the influence of atmospheric rivers, precipitation is more abundant, which was reflected in both IMERG data and gauge observations. Past studies have shown that the precipitable water and integrated water vapor fluxes over this area were largely enhanced by the negative anomalies in sea level pressure and upper-level height in the central Pacific [62]. The variability in atmospheric river frequency can drive hydrometeorological extremes with broad societal impacts over the Pacific Northwest of North America [63]. To the east of 100°W, the frequent tropical cyclones and cold fronts result in higher precipitation, as revealed by values exceeding 800 mm/y annually in most areas and reaching up to 1400 mm/y in the southeastern regions.

In Europe, despite the few selected grid points, the annual precipitation total estimates derived from IMERG were still quite consistent with gauge observations. On average, the average RB in the annual precipitation total records from 2001 to 2020 at almost all stations was larger than zero, indicating that IMERG generally overestimated this parameter. Spatially, the RB between IMERG data and gauge observations was larger in regions with lower annual precipitation totals, such as the northwestern regions of China and parts of

the western United States, where it exceeded 30%, and even reached 50% in some grids. In other regions, the RB of most grids was less than 10%.

Figure 3 shows that the precipitation frequency estimated by IMERG was significantly higher than that obtained from meteorological stations, especially in northern China and western America. This discrepancy may be attributed to the fact that GPM products are capable of detecting light rainfall and solid precipitation events. Previous assessments have also demonstrated the clear improvement achieved in the IMERG precipitation product in comparison with its predecessor, especially in reducing missed precipitation and hit bias in winter, revealing the general superiority of GPM IMERG [44,64]. However, due to differences in data sources, observation methods, and spatial scales, a certain bias was detected between IMERG data and gauge observations. Specifically, in China, IMERG data overestimated the precipitation frequency in the northern region by approximately 4% compared to gauge observations, with RB values reaching up to 100% in some areas. This could be due to the complex atmospheric circulation and convective precipitation in northern China [65,66], leading to errors in the GPM inversion of these complex processes. Similarly, in western America, IMERG overestimated the precipitation frequency overall, with the RB values in most grids exceeding 40% and reaching up to 100% in some cases. This may be related to the complexity of the terrain and the influence of atmospheric circulation near the Pacific Ocean. The precipitable water and integrated water vapor fluxes over this area derived from the atmospheric river and were blocked by the Rocky Mountains, resulting in plentiful precipitation [62]. It was found that the IMERG precipitation records in this area were related to the documented low detection rate of satellites and to over arid/semiarid areas with hot background surfaces [19,67].

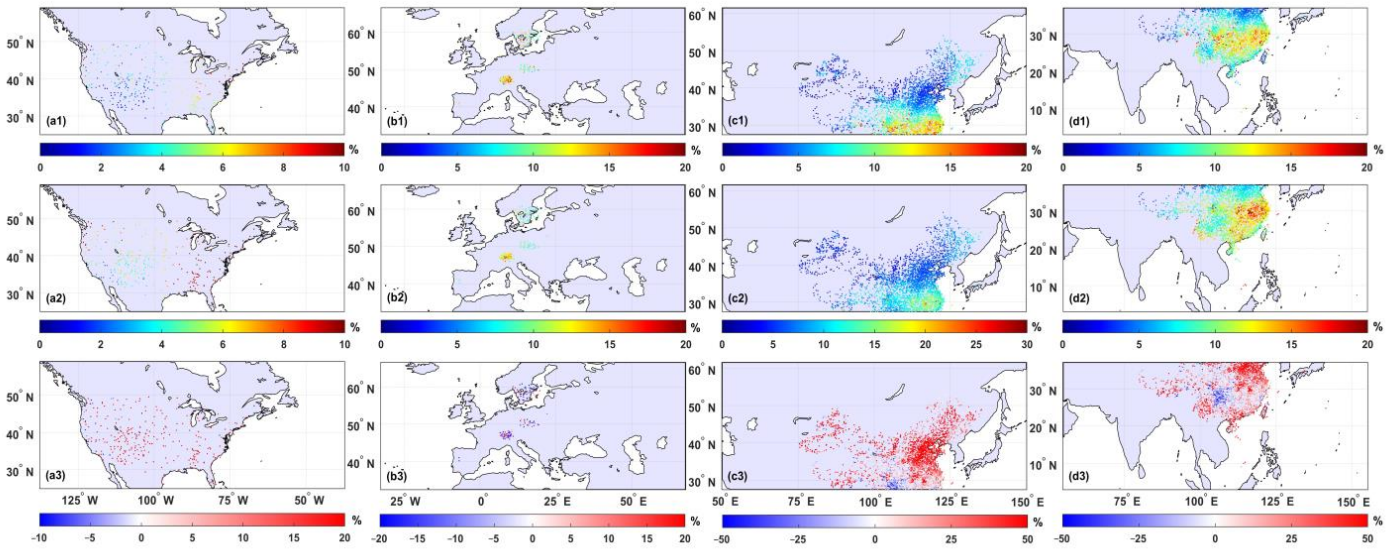

Figure 3. Average annual precipitation frequency from 2001 to 2020 obtained from gauge observations (**a1**–**d1**) and IMERG data (**a2**–**d2**), and the bias of IMERG data relative to gauge observations (**a3**–**d3**), for North America, Europe, North Asia, and South Asia, respectively.

Significant overestimation biases were also identified between IMERG data and gauge observations in terms of the spatial distribution of high-frequency rainfall events. In China, IMERG estimated high-frequency rainfall in the Yangtze-Huaihe River basin, with annual precipitation frequencies as high as 20%. Gauge observations, on the other hand, revealed a belt-like area characterized by high-frequency precipitation in this region, possibly due to its climatic characteristics and topographical conditions. Conversely, IMERG underestimated the precipitation frequency in the Sichuan Basin, possibly due to the limitations of this technology in accurately simulating complex terrain and precipitation systems. In Europe, IMERG provided good estimates of precipitation frequency, largely replicating the spatial patterns of gauge observations, with RB values below 20%. This was likely because the

climate in Europe is relatively temperate, and the atmospheric circulation and precipitation systems can be reversed more accurately, resulting in a higher consistency between IMERG data and gauge observations.

Figure 4 illustrates noticeable discrepancies in the estimates of precipitation intensity derived from IMERG compared to gauge observations across different regions. In both China and America, IMERG tended to underestimate high-intensity precipitation events. In southern China and the Beijing-Tianjin-Hebei region, IMERG could identify the areas characterized by high-intensity precipitation, but the maximum detected frequency reached only 2 mm/h, which was approximately 0.5 mm/h lower than that measured at meteorological stations. This led to IMERG data having an overall negative RB of up to −50%, particularly in the Beijing-Tianjin-Hebei region. A similar situation was observed in the southeastern United States, where the IMERG data for precipitation intensity were spatially consistent with gauge observations, but the former technology underestimated the magnitude. Conversely, in the Sichuan Basin, China, IMERG overestimated the hourly precipitation intensity but underestimated the precipitation frequency. For areas where precipitation intensity exceeded 1.5 mm/h, the RBs in this parameter reached 50%. In Europe, the IMERG estimates of precipitation intensity were notably higher than gauge observations. This overestimation could be attributed to the higher estimates of average annual precipitation totals in Europe and the good performance of IMERG in estimating annual precipitation frequencies.

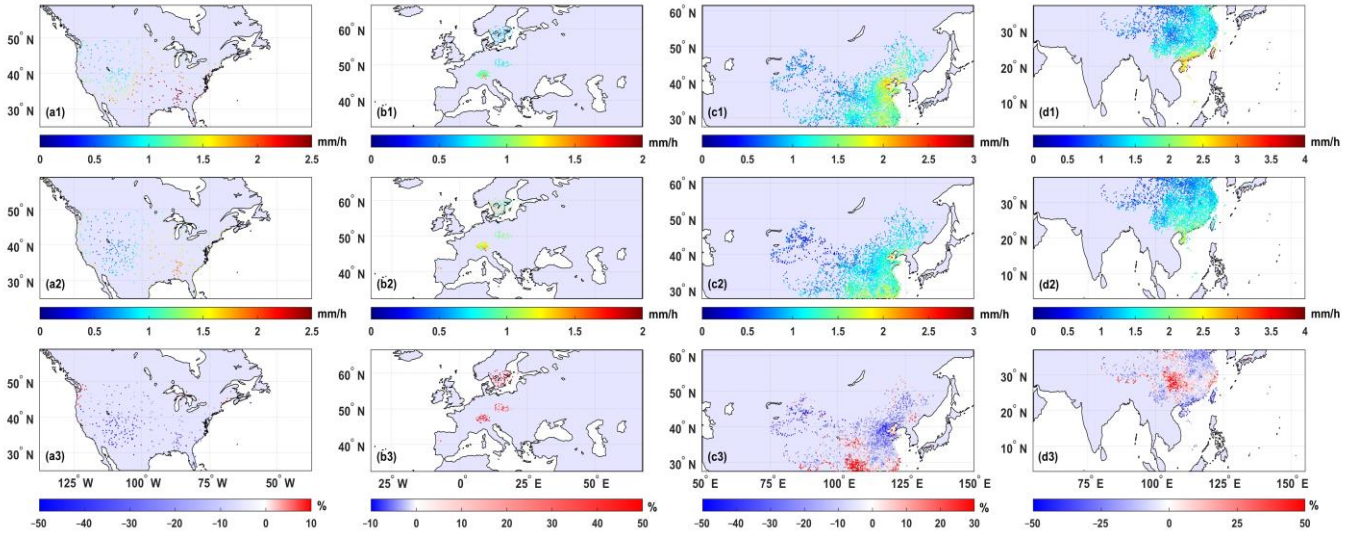

Figure 4. Average annual precipitation intensity from 2001 to 2020 obtained from gauge observations (**a1**–**d1**) and IMERG data (**a2**–**d2**), and the bias of IMERG data relative to gauge observations (**a3**–**d3**), for North America, Europe, North Asia, and South Asia, respectively.

3.2. Analysis of Errors in IMERG Precipitation Data

To further evaluate the errors in the IMERG estimates of hourly precipitation and investigate the correlation between IMERG data and gauge observations, the two datasets obtained for the four regions examined over the study period were ranked by the observation hours. Then, three metrics, i.e., CC, MAE, and RMSE, were calculated to analyze the variability of hourly precipitation for these two time series with same length.

Table 2 shows that the correlation between IMERG data and gauge observations clearly varied across different regions. Notably, the lowest CC (0.308) was observed for European stations. However, in this region, IMERG data exhibited the smallest RMSE of 0.761 mm/h when compared to gauge observations. This discrepancy may be attributed to the prevalence of light rainfall and higher precipitation frequencies in Europe, resulting in a poorer correlation but smaller RMSE. In comparison, the CC for South Asia is 0.350, and higher RMSE and MAE values were obtained in this region, possibly due to the

predominance of extremely intense convective rainfall. Similar CC values were obtained for North America (0.367) and North Asia (0.373). The RMSE and MAE values were also comparable between these regions. This was likely due to their geographical proximity and similar climatic conditions within the same latitude belt. Additionally, the higher number of meteorological stations in North Asia contributed to the better correlation between IMERG data and gauge observations.

3.3. Validating the Quality of IMERG Data Based on Diurnal Variations

Figure 5 illustrates the diurnal variation of the average annual cycle of hourly precipitation amount, frequency, and intensity for the four regions examined. In terms of total precipitation (top row in Figure 5), both gauge observations and IMERG data showed distinct diurnal patterns across the four regions. In North America, IMERG data were quite consistent with gauge observations, with precipitation peaking at 23:00 UTC and reaching minimal values around 15:00–16:00 UTC. However, IMERG tended to overestimate the peak-hour precipitation (41 mm/h for gauge observations and 44 mm/h for IMERG data) and underestimate the trough-hour precipitation (30 mm/h for gauge observations and 28 mm/h for IMERG data). IMERG could adequately reflect the diurnal cycle of hourly precipitation in spite of the above-mentioned overestimation and underestimation, which may be related to local effects associated with the terrain.

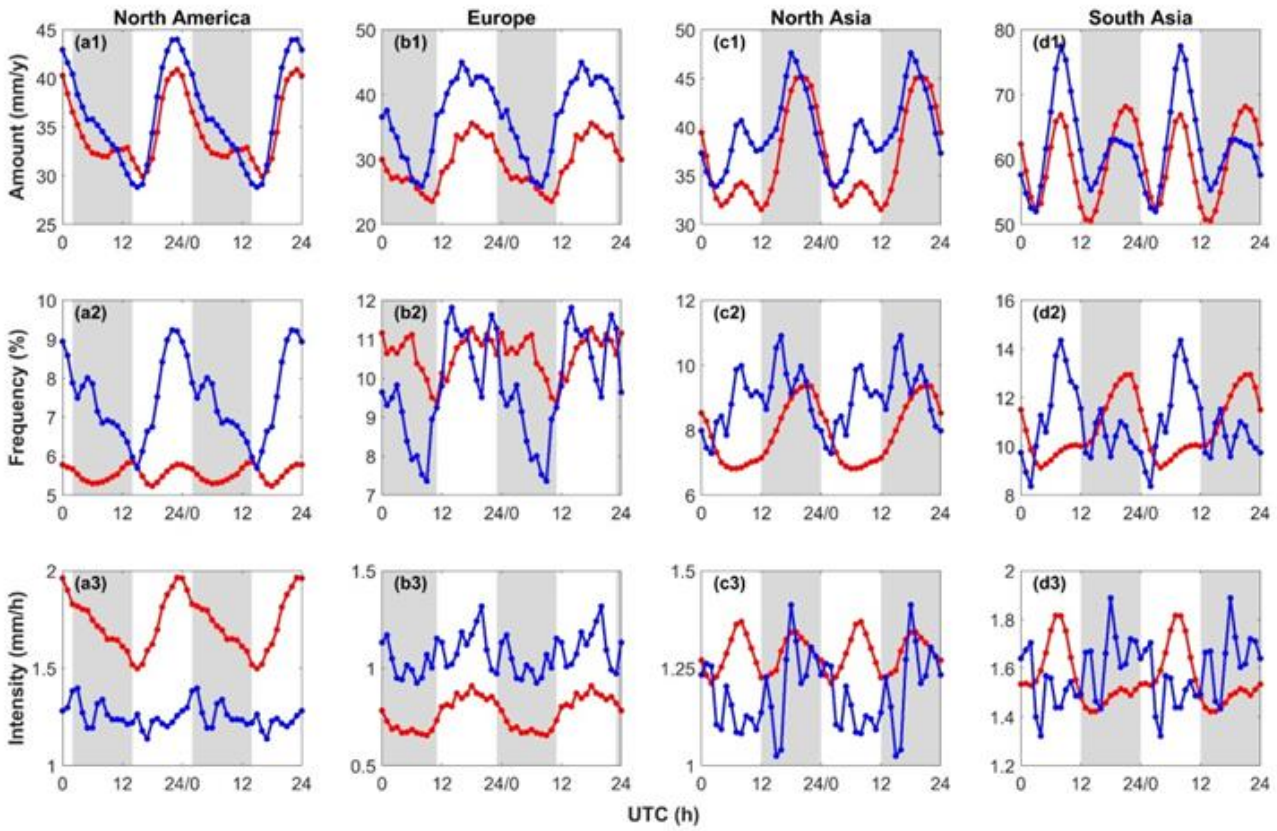

Figure 5. Diurnal variation of average annual cycle of hourly precipitation amount (**top row**), precipitation frequency (**middle row**), and precipitation intensity (**bottom row**) for different regions; the red and blue lines represent gauge observations and IMERG data, respectively; (**a**) North America, (**b**) Europe, (**c**) North Asia, and (**d**) South Asia. The shadow represents the nighttime (20:00–08:00) for the local time.

In Europe, IMERG generally overestimated the diurnal cycle of hourly precipitation, especially at peak hours (35 mm/h for gauge observations and 45 mm/h for IMERG data), with mismatched phases between these two datasets. Distinct bimodal patterns of precipi-

tation intensity were detected in South Asia, but IMERG overestimates a small variation in North Asia. The peak structures observed in IMERG was close to observation in South Asia but showed a large disparity at around 09:00 in North Asia. This disparity may be related to the systematic problem with satellite inversion in terms of precipitation frequency and intensity. Many drizzles can evaporate into the air before the small raindrops arriving at the ground, thus not being captured by the rain gauge, especially at daytime. However, the satellite estimates precipitation from the scattering of ice crystals in the clouds, resulting much larger frequency but smaller intensity for IMERG data than gauge observation.

The ability of the IMERG product to detect precipitation at different hours for the four regions examined is shown in Figure 6. The regional mean values of POD, FAR and CSI are listed in Table 2. POD values fluctuating around approximately 50% throughout the day were detected in each region. Specifically, in North America, the peak daily precipitation occurred at 16:00 local time, with POD reaching about 55%. High precipitation rates were maintained between 16:00 and 23:00 local time, declining thereafter until reaching a minimum around 10:00 the next day (POD of approximately 45%). In contrast, in Europe, the lowest POD for hourly precipitation (around 35%) was detected around 11:00 local time and then increased to a maximum of 45% at 11:00 local time. Then, the POD values remained near 45% until 06:00 the next day. In North Asia, three peak POD values were detected at 19:00, 23:00, and 04:00 local time. The difference in POD between daytime and nighttime, which ranged from 50% to 55%, was not significant, possibly due to the high nighttime precipitation in the Sichuan Basin boosting the POD values at this time. In contrast, a distinct diurnal variation was detected in North Asia, with a peak POD value of approximately 57% at around 16:00 local time and dropping to a minimum of 45% at around 02:00 the next day.

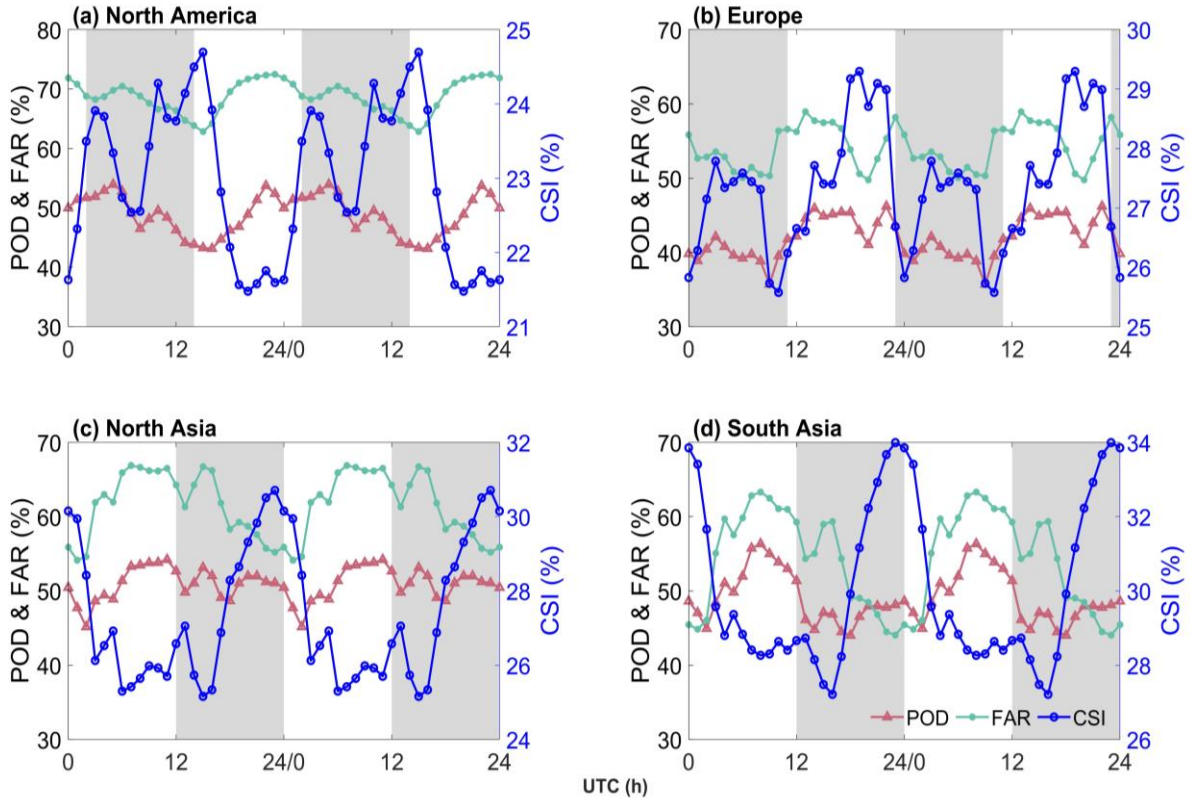

Figure 6. Diurnal precipitation cycle measured via the following parameters: Probability of Detection (POD), False Alarm Ratio (FAR), and Critical Success Index (CSI); the red and green lines represent POD and FAR, respectively, with ranges being shown on the left axis; the blue line represents CSI, with the range being shown on the right axis. The shadow represents the nighttime (20:00–08:00) for the local time.

The diurnal cycle of FAR in all regions examined showed a similar pattern to that of POD. Similar CSI patterns were observed in North America, North Asia, and South Asia, with values peaking around 08:00 local time and decreasing in the afternoon. This may be due to morning weather conditions being conducive to lower errors in remote sensing observations.

3.4. Validation of IMERG Data Quality Based on Interannual Variability

Figure 7 shows the comparisons of the interannual variability of annual precipitation total, frequency, and intensity between IMERG data and gauge observations for the four regions examined. IMERG overestimated total precipitation in individual years, but the data were consistent with gauge observations for all the four regions. This may be due to the fact that the IMERG data had been corrected based on monthly ground precipitation observations. The discrepancy was slightly larger in Europe, possibly because of the sparse grid network used in this study leading to larger errors in IMERG data. The average annual precipitation total in North America, Europe, and North Asia varied between 500 mm/y and 1000 mm/y. A significant upward trend was detected in this parameter in North America, which increased from over 500 mm/y in 2001 to around 1000 mm/y in 2020, possibly due to climate change. Indeed, the water cycle or specific regional topography and circulation patterns in this region would be strengthened under global warming. Conversely, the annual precipitation total in North Asia decreased from 1000 mm/y in 2001 to 750 mm/y in 2020. This could be attributed to widespread human activities associated with land use and land cover changes. Due to its geographical location and monsoon system, South Asia exhibited a considerably higher annual precipitation total compared with the other three regions, with values fluctuating around 1200 mm/y and significant interannual variability.

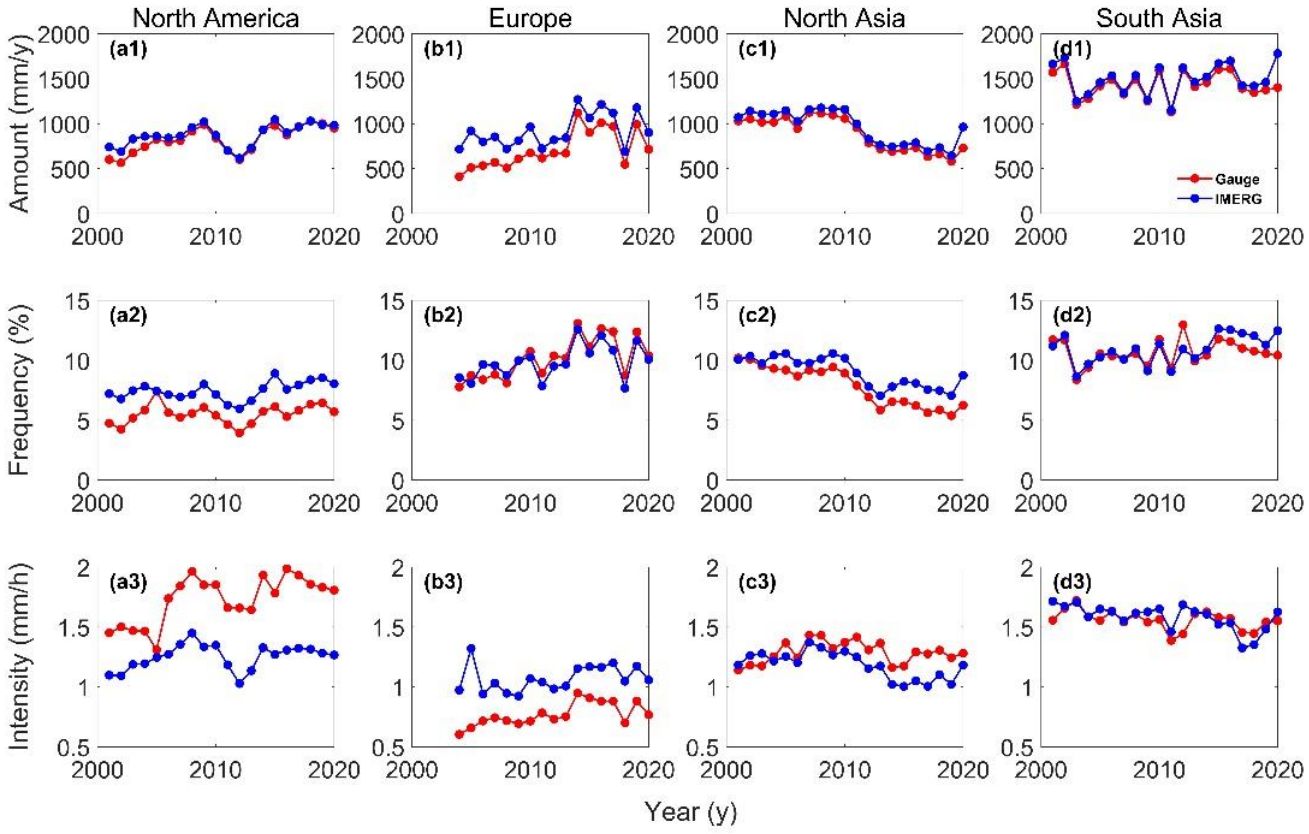

Figure 7. Interannual variations in regional annual precipitation total (**first row**), precipitation frequency (**second row**), and hourly precipitation intensity (**third row**). In these plots, the red and blue lines represent gauge observations and IMERG data, respectively. Panels (**a**–**d**) correspond to North America, Europe, North Asia, and South Asia, respectively.

IMERG overestimated the annual precipitation frequency in North America and North Asia by 2.5% and 2%, respectively, and the two regions showed an increasing and decreasing trend in this parameter, also respectively. The IMERG data obtained for Europe in terms of interannual precipitation variability matched well to the gauge observations, although these were slightly higher than the IMERG estimates. In terms of the hourly precipitation intensity, IMERG data performs best in South Asia, fluctuating around 1.7 mm/h. However, in North Asia and North America, IMERG generally underestimated precipitation intensity, while it overestimated precipitation frequency. In North Asia, the difference was minimal (1.25 mm/h), while in North America, it was pronounced, exceeding 1 mm/h. In Europe, as observed for total precipitation, IMERG overestimated precipitation intensity by 0.25 mm/h compared to gauge observations.

Figure 8 shows the interannual variations in precipitation in the four regions examined as measured by the three above-mentioned qualitative indicators, i.e., POD, FAR, and CSI. POD exhibited an upward trend in each region, with the values in North America, South Asia, and North Asia all exceeding 50% in the later years of the study period, while a lower POD of around 40% was observed in Europe. FAR showed a decreasing trend in North America and Europe, and this may attribute to the small number of meteorological stations in the early stage of the study period. Conversely, a clear increasing trend in this parameter was observed in North Asia and South Asia, possibly due to the increased difficulty in accurately measuring precipitation amid the rise of extreme precipitation events associated with global warming. CSI, which reflects the trends in both POD and FAR, showed an increasing trend in North America and Europe. In the Asian regions, this index exhibited a downward trend, particularly in North Asia, where it decreased from around 30% in 2001 to approximately 26% in 2020.

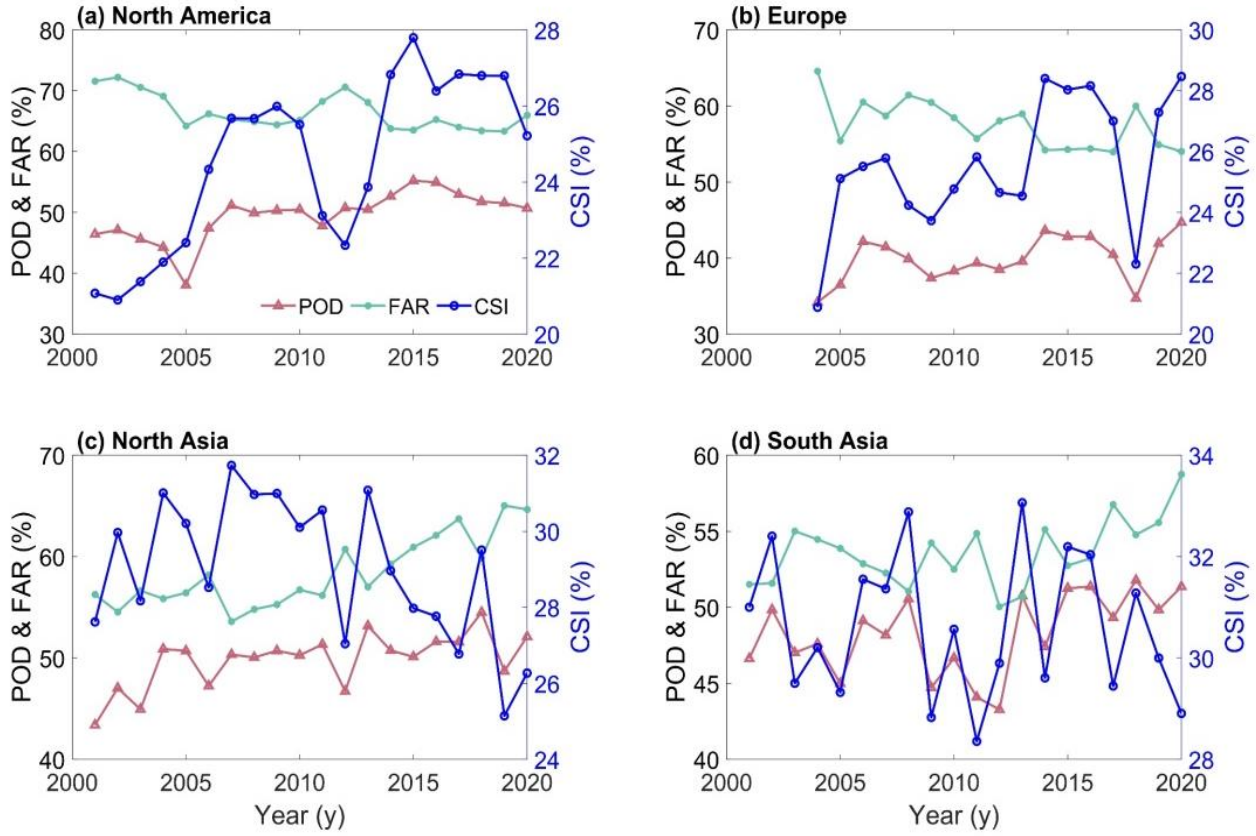

Figure 8. Interannual variations in regional precipitation measured using the Probability of Detection (POD), False Alarm Ratio (FAR), and Critical Success Index (CSI). In these plots, the red and green lines represent POD and FAR, respectively, with their variation ranges on the left y-axis. The blue line represents the CSI, with its variation range on the right y-axis.

4. Discussion

4.1. Superiority of IMERG Product

The GPM satellite is equipped with a dual-frequency precipitation radar and integrates active radar observation technology to enhance its ability to detect light rain and solid precipitation. It can provide multi-angle information on cloud precipitation particles, enabling monitoring at a high spatiotemporal resolution and the analysis of precipitation at the global scale. Among various GPM products for the analysis of precipitation, IMERG-F is corrected by ground station observations, and usually the quality of its data is superior to that of other products [33]. Nonetheless, satellite data are somewhat inaccurate, since they estimate ground precipitation via an indirect method [1,3,68]. Therefore, numerous studies have attempted to evaluate the spatiotemporal patterns and variability of IMERG data by comparing them with observations derived from meteorological stations [17,19,26,58,69]. Although tropical ocean regions account for the majority of global precipitation, there are almost no meteorological stations over the ocean, meaning that the satellite inversion can only be validated using data obtained from land-based stations [8,70]. The contribution of this study is compressively evaluating GPM IMERG products using a wider range of gauge observation data at the hourly scale and over the latest two decades. The new findings emphasized the changes of precipitation at hourly scale and the improvement of detectability, under the comparisons of IMERG product performances over different regions.

Although many research institutions run precipitation monitoring projects based on data obtained from meteorological stations, few of these are available at the hourly scale. Hourly precipitation data can provide information to elucidate the mechanism underlying the development of extreme precipitation events and their occurrence, whereas such insights may be lost by averaging values over entire days [71–73]. In this study, hourly precipitation data from the ISD, CMA, and U.S. USCRN datasets were used as a test bed to compressively validate the GPM IMERG product over the globe. Specifically, precipitation amount, frequency, and intensity were evaluated as they are crucial parameters for describing precipitation and play key roles in climate research, water resource management, and disaster prevention. The accuracy and reliability of the IMERG estimates of these parameters across different regions were compared with hourly precipitation observations obtained from ground stations between 2001 and 2020. Due to the estimate obtained from infrared band calibrated by microwaves, IMERG was found to facilitate the detection of light and solid precipitation [17,26].

4.2. Discrepancies in Precipitation Frequency and Intensity

The analysis in this study revealed that IMERG data and gauge observations exhibited similar spatial distribution characteristics, particularly in Asia and the United States. This was mainly due to the improved inversion ability of the new-generation GPM product, which can detect light rain and solid precipitation [34,35,42]. However, IMERG slightly overestimated annual precipitation amounts (especially in regions experiencing lower annual precipitation), with data exhibiting relatively larger deviations compared to ground station observations. Similar overestimations of IMERG data in precipitation have also been reported [34]. Significant deviations in precipitation frequency were observed in northern China and western United States, while IMERG performed well in estimating this parameter in the European region. This may be related to the fact that, due to oceanic climate condition, the seasonal distribution of precipitation frequency is relatively even [73,74]. In terms of precipitation intensity, IMERG data showed noticeable deviations from gauge observations across different regions, underestimating high precipitation intensity in China and the United States but overestimating it in Europe. This disparity may be related to the evaporation of small raindrops before arriving at the ground, and therefore many drizzles cannot be captured by the rain gauge, which can be identified by the remote sensors from the scattering of ice crystals in the clouds [12]. Past studies in a predominantly tropical region also attributed the low performance of IMERG precipitation intensity to the difficulty in estimating precipitation from warm clouds [75]. The results are in line with previous

studies where precipitation frequency was also overestimated while the intensity was underestimated, leading to annual precipitation amounts that were comparable with those derived from gauge observations [21,37].

The diurnal cycle of precipitation is an important feature in hydrometeorological studies and also is a key aspect in the evaluation of satellite precipitation products with a high spatial-temporal resolution [21,72]. This study also evaluated the detectability of GPM IMERG products in reproducing the diurnal cycle of precipitation using several quantitative and qualitative statics. It was found that IMERG data and gauge observations described very similar diurnal precipitation cycles in South Asia. However, the former overestimated precipitation at peak hours but underestimated it at trough hours in North America, and generally overestimated the diurnal variations (with a large degree of overestimation at peak hours) in Europe and North Asia. This may be related to the influence of climatic factors and the fact that these areas are prone to experience heavy rainfall, especially in the summer [25,72]. The two datasets showed similar patterns of fluctuation of the hourly precipitation frequency in the four regions examined, although the daily fluctuation for this parameter in IMERG data was large, while gauge observations fluctuated more stably. The POD of hourly precipitation in each region generally fluctuated around 50%. Gauge observations have been demonstrated to reflect rather stable precipitation frequencies and intensities during the diurnal cycle, while IMERG data have shown strong fluctuations mainly because of inaccurate estimates from the cross-track microwave sensors at individual hours [21].

In terms of the interannual variation in annual precipitation total, IMERG data and gauge observations showed similar trends due to the correction of the former dataset using monthly ground observations [7,33,55]. Both datasets detected a clear increasing trend in annual precipitation total in North America and a downward trend in North Asia. This is basically consistent with the variation in the annual precipitation frequency in these areas. The POD values for IMERG data in each selected region showed an increasing trend, which is due to the improved GPM sensors compared with previous versions [17,26]. In terms of the interannual variability of hourly precipitation intensity, IMERG data and gauge observations showed the highest consistency in South Asia, which may be related to the high precipitation intensity characterizing the climate in this region, a feature that is thus more easily detected.

4.3. Effects of Monitoring Station Density

As the IMERG product is area-averaged and gauge observation is point time series, the representativeness of these two datasets are essentially different. This directly compared the gauge observation with the grid data in which the station is located. For a grid with more than one station, the precipitation metrics are calculated for each station, and then the averaged values for all the stations in this grid are used as the grid observation. Therefore, the IMERG product is certainly closer to the gauge observation for the grid with more meteorological stations. The evaluation results in this study showed IMERG performs differently over different regions, possibly due to the density of monitoring stations.

Past works have illustrated that the station density is the major factor in the validation of grid precipitation product, especially in complex terrain areas [76]. To illustrate this point, the average number of meteorological stations within each $0.1^\circ \times 0.1^\circ$ grid was calculated. It demonstrated that most of the grids have only one station, and few of them have two. The gauge observations in the grid with more stations are preferable to mitigate the inherently different between the grid product and point time series. It was shown that Europe (152 stations in 144 grids) and North Asia (1786 stations in 1436 grids) had the lowest and highest station densities, respectively. This situation could potentially hinder the evaluation of IMERG products in Europe as a whole. Therefore, the analysis outcomes would seem more reliable in the Chinese domain, where more stations are available to use for validation. Satellite precipitation products still have large uncertainty in estimating precipitation over areas with sparsely distributed stations [15].

4.4. Effects of Reference Value

Since precipitation is a non-normal distributed variable, especially at an hourly scale, the selected reference value may have a certain impact on the evaluation results. This study involved the reference value of 0.1 mm/h for IMERG data, to ensure the consistency with the minimum value that the rain gauge could detect. Some studies of extreme weather indices focused on a reference value of 1 mm/day, which excluded the days with very light precipitation [77,78]. To detect the uncertainty caused by different reference value, the statistics were recalculated using the reference value of 0.5 mm/h. The regional mean POD is 40.2%, 40.0%, 47.1%, 49.4%, and FAR is 66.7%, 60.8%, 63.6%, 60.3% for North America, Europe, North Asia and South Asia, respectively. It shows that these metrics are insensitive to the reference value. However, the MAE and RMSE are much larger for the case of 0.5 mm/h than for 0.1 mm/h, due to the large magnitude and low frequency of precipitation in both gauge observation and IMERG data under the large truncation.

Actually, precipitation is a discontinuous variable largely affected by many thermal and dynamic factors, which cause its intermittency and fluctuation at nearly all temporal and spatial scales. Although the evaluation conducted in this study was based on an hourly time scale, it essentially adopted the equal-time-interval method. Alternatively, the event-based evaluation method would provide more information, reflecting the discontinuity of precipitation [16,48,79]. In the future research, we plan to use more precipitation data and other assessment methods to reveal water vapor sources and the mechanisms regulating global precipitation. Moreover, we will investigate the error associated with satellite precipitation products in different climatic regions than the geographical zone examined in this study.

5. Conclusions

In summary, the comparison of hourly precipitation data obtained from GPM IMERG and gauge observations revealed largely consistent spatial patterns of annual precipitation total but disparities in the patterns of annual precipitation frequency and intensity. The highest and lowest correlations between the two datasets for hourly precipitation were detected in North Asia (0.373, $p < 0.05$) and Europe (0.308, $p < 0.05$), respectively. Hourly precipitation intensity showed the largest RMSE (1.29 mm/h) in South Asia due to the strong precipitation intensity characterizing this region. IMERG was able to capture the bimodal structure of diurnal precipitation in South Asia but performed a small variation in North Asia. It generally overestimated precipitation at peak hours and underestimated it at trough hours, which resulted in larger fluctuations in the data compared with gauge observations. Both datasets showed similar patterns of interannual precipitation variability after the correction of the IMERG data using monthly ground observations, but IMERG overestimated the proportion of annual precipitation hours by 2.5% and 2.0% in North America and North Asia, respectively. These findings provide valuable insights for weather forecasting, the identification of extreme weather events, and climate change research.

Author Contributions: Conceptualization, G.W.; methodology, P.L. and G.W.; software, P.L.; validation, P.L.; formal analysis, P.L.; investigation, G.W.; resources, G.W.; data curation, G.W.; writing—original draft preparation, P.L. and G.W.; writing—review and editing, P.L. and G.W.; visualization, P.L.; supervision, G.W.; project administration, G.W.; funding acquisition, G.W. All authors have read and agreed to the published version of the manuscript.

Funding: This research was funded by the National Natural Science Foundation of China (42077421 and 41930970).

Data Availability Statement: The precipitation data of Integrated Surface Database (ISD) were downloaded from https://www.ncei.noaa.gov/products/land-based-station/integrated-surface-database (accessed on 14 June 2023). The hourly precipitation data from China Meteorological Administration (CMA) were available at http://data.cma.cn/en/?r=data/detail&dataCode=A.0012.0001 (accessed on 7 July 2023). The hourly precipitation data from the U.S. Climate Reference Network (USCRN) were available at https://www.ncei.noaa.gov/access/crn/ (accessed on 20 November

2023). The GPM IMERG product data from 2001 to 2020 were downloaded at https://pmm.nasa.gov/data-access/downloads/gpm (accessed on 13 January 2022).

Conflicts of Interest: The authors declare no conflicts of interest.

References

1. Kidd, C.; Huffman, G.; Maggioni, V.; Chambon, P.; Oki, R. The Global Satellite Precipitation Constellation: Current status and future requirements. *Bull. Am. Meteorol. Soc.* **2021**, *102*, E1844–E1861. [CrossRef]
2. Xie, P.; Xiong, A. A conceptual model for constructing high-resolution gauge-satellite merged precipitation analyses. *J. Geophys. Res. -Atmos.* **2011**, *116*, D21106. [CrossRef]
3. Kidd, C.; Levizzani, V. Status of satellite precipitation retrievals. *Hydrol. Earth Syst. Sci.* **2011**, *15*, 1109–1116. [CrossRef]
4. Fu, Y.; Jiang, S.; Mao, Y.; Wu, G. Urbanization reshapes extreme precipitation metrics in typical urban agglomerations of Eastern China. *Atmos. Res.* **2024**, *300*, 107253. [CrossRef]
5. Lin, M.; Huybers, P. If Rain Falls in India and No One Reports It, Are Historical Trends in Monsoon Extremes Biased? *Geophys. Res. Lett.* **2019**, *46*, 1681–1689. [CrossRef]
6. Maggioni, V.; Meyers, P.C.; Robinson, M.D. A Review of Merged High-Resolution Satellite Precipitation Product Accuracy during the Tropical Rainfall Measuring Mission (TRMM) Era. *J. Hydrometeorol.* **2016**, *17*, 1101–1117. [CrossRef]
7. Tang, G.; Clark, M.P.; Papalexiou, S.M.; Ma, Z.; Hong, Y. Have satellite precipitation products improved over last two decades? A comprehensive comparison of GPM IMERG with nine satellite and reanalysis datasets. *Remote Sens. Environ.* **2020**, *240*, 111697. [CrossRef]
8. Adler, R.F.; Gu, G.; Sapiano, M.; Wang, J.J.; Huffman, G.J. Global Precipitation: Means, Variations and Trends During the Satellite Era (1979–2014). *Surv. Geophys.* **2017**, *38*, 679–699. [CrossRef]
9. Sun, Q.H.; Miao, C.Y.; Duan, Q.Y.; Ashouri, H.; Sorooshian, S.; Hsu, K.L. A Review of Global Precipitation Data Sets: Data Sources, Estimation, and Intercomparisons. *Rev. Geophys.* **2018**, *56*, 79–107. [CrossRef]
10. Benitez, V.D.; Forgioni, F.P.; Lovino, M.A.; Sgroi, L.; Doyle, M.E.; Müller, G.V. Capability of satellite data to estimate observed precipitation in southeastern South America. *Int. J. Climatol.* **2024**, *44*, 792–811. [CrossRef]
11. Harrison, L.; Funk, C.; Peterson, P. Identifying changing precipitation extremes in Sub-Saharan Africa with gauge and satellite products. *Environ. Res. Lett.* **2019**, *14*, 085007. [CrossRef]
12. Li, Y.; Guo, B.; Wang, K.; Wu, G.; Shi, C. Performance of TRMM Product in Quantifying Frequency and Intensity of Precipitation during Daytime and Nighttime across China. *Remote Sens.* **2020**, *12*, 740. [CrossRef]
13. Wu, G.; Zhao, R.; Ma, Z.; Shi, C. The hourly precipitation intensity and frequency in the Yarlung Zangbo river basin in China during last decade. *Meteorol. Atmos. Phys.* **2020**, *132*, 899–907. [CrossRef]
14. Zhou, C.G.; Gao, W.; Hu, J.R.; Du, L.M.; Du, L. Capability of IMERG V6 Early, Late, and Final Precipitation Products for Monitoring Extreme Precipitation Events. *Remote Sens.* **2021**, *13*, 689. [CrossRef]
15. Huang, A.M.; Zhao, Y.; Zhou, Y.; Yang, B.; Zhang, L.; Dong, X.; Fang, D.; Wu, Y. Evaluation of multisatellite precipitation products by use of ground-based data over China. *J. Geophys. Res.-Atmos.* **2016**, *121*, 10654–10675. [CrossRef]
16. Li, R.; Wang, K.; Qi, D. Event-Based Evaluation of the GPM Multisatellite Merged Precipitation Product From 2014 to 2018 Over China: Methods and Results. *J. Geophys. Res.-Atmos.* **2021**, *126*, e2020JD033692. [CrossRef]
17. Xu, F.; Guo, B.; Ye, B.; Ye, Q.; Chen, H.; Ju, X.; Guo, J.; Wang, Z. Systematical Evaluation of GPM IMERG and TRMM 3B42V7 Precipitation Products in the Huang-Huai-Hai Plain, China. *Remote Sens.* **2019**, *11*, 697. [CrossRef]
18. Tsitelashvili, N.; Biggs, T.; Mu, Y.; Trapaidze, V. Regional Precipitation Regimes and Evaluation of National Precipitation Datasets Against Satellite-Based Precipitation Estimates, Republic of Georgia. *J. Hydrometeorol.* **2024**, *25*, 591–600. [CrossRef]
19. Li, R.; Guilloteau, C.; Kirstetter, P.E.; Foufoula-Georgiou, E. How well does the IMERG satellite precipitation product capture the timing of precipitation events? *J. Hydrol.* **2023**, *620*, 129563. [CrossRef]
20. Wang, N.; Liu, W.; Sun, F.; Yao, Z.; Wang, H.; Liu, W. Evaluating satellite-based and reanalysis precipitation datasets with gauge-observed data and hydrological modeling in the Xihe River Basin, China. *Atmos. Res.* **2020**, *234*, 104746. [CrossRef]
21. Li, R.; Wang, K.; Qi, D. Validating the Integrated Multisatellite Retrievals for Global Precipitation Measurement in Terms of Diurnal Variability With Hourly Gauge Observations Collected at 50,000 Stations in China. *J. Geophys. Res. -Atmos.* **2018**, *123*, 10423–10442. [CrossRef]
22. Sapiano, M.R.P.; Arkin, P.A. An Intercomparison and Validation of High-Resolution Satellite Precipitation Estimates with 3-Hourly Gauge Data. *J. Hydrometeorol.* **2009**, *10*, 149–166. [CrossRef]
23. Dollan, I.J.; Maina, F.Z.; Kumar, S.V.; Nikolopoulos, E.I.; Maggioni, V. An assessment of gridded precipitation products over High Mountain Asia. *J. Hydrol.-Reg. Stud.* **2024**, *52*, 101675. [CrossRef]
24. McCollum, J.R.; Krajewski, W.F.; Ferraro, R.R.; Ba, M.B. Evaluation of biases of satellite rainfall estimation algorithms over the continental United States. *J. Appl. Meteorol.* **2002**, *41*, 1065–1080. [CrossRef]
25. Ashouri, H.; Sorooshian, S.; Hsu, K.L.; Bosilovich, M.G.; Lee, J.; Wehner, M.F.; Collow, A. Evaluation of NASA's MERRA Precipitation Product in Reproducing the Observed Trend and Distribution of Extreme Precipitation Events in the United States. *J. Hydrometeorol.* **2016**, *17*, 693–711. [CrossRef]

26. Liu, Z. Comparison of Integrated Multisatellite Retrievals for GPM (IMERG) and TRMM Multisatellite Precipitation Analysis (TMPA) Monthly Precipitation Products: Initial Results. *J. Hydrometeorol.* **2016**, *17*, 777–790. [CrossRef]
27. Romilly, T.G.; Gebremichael, M. Evaluation of satellite rainfall estimates over Ethiopian river basins. *Hydrol. Earth Syst. Sci.* **2011**, *15*, 1505–1514. [CrossRef]
28. Hosseini-Moghari, S.-M.; Tang, Q. Can IMERG Data Capture the Scaling of Precipitation Extremes with Temperature at Different Time Scales? *Geophys. Res. Lett.* **2022**, *49*, e2021GL096392. [CrossRef]
29. Kubota, T.; Ushio, T.; Shige, S.; Kida, S.; Kachi, M.; Okamoto, K. Verification of High-Resolution Satellite-Based Rainfall Estimates Around Japan Using a Gauge-Calibrated Ground-Radar Dataset. *J. Meteorol. Soc. Jpn.* **2009**, *87A*, 203–222. [CrossRef]
30. Duncan, J.M.A.; Biggs, E.M. Assessing the accuracy and applied use of satellite-derived precipitation estimates over Nepal. *Appl. Geogr.* **2012**, *34*, 626–638. [CrossRef]
31. Rachdane, M.; El Khalki, E.; Saidi, M.E.; Nehmadou, M.; Ahbari, A.; Tramblay, Y. Comparison of High-Resolution Satellite Precipitation Products in Sub-Saharan Morocco. *Water* **2022**, *14*, 3336. [CrossRef]
32. Li, X.Y.; Sungmin, O.; Wang, N.; Liu, L.C.; Huang, Y.Z. Evaluation of the GPM IMERG V06 products for light rain over Mainland China. *Atmos. Res.* **2021**, *253*, 105510. [CrossRef]
33. Huffman, G.J.; Bolvin, D.T.; Braithwaite, D.; Hsu, K.; Joyce, R.; Kidd, C.; Nelkin, E.J.; Sorooshian, S.; Tan, J.; Xie, P.P. NASA Global Precipitation Measurement (GPM) Integrated Multi-SatellitE Retrievals for GPM (IMERG) Algorithm Theoretical Basis Document (ATBD) Version 06. 2020. Available online: https://gpm.nasa.gov/sites/default/files/2020-05/IMERG_ATBD_V06.3.pdf (accessed on 27 September 2024).
34. Wang, Y.; Miao, C.; Zhao, X.; Zhang, Q.; Su, J. Evaluation of the GPM IMERG product at the hourly timescale over China. *Atmos. Res.* **2023**, *285*, 106656. [CrossRef]
35. Pradhan, R.K.; Markonis, Y.; Godoy, M.R.V.; Villalba-Pradas, A.; Andreadis, K.M.; Nikolopoulos, E.I.; Papalexiou, S.M.; Rahim, A.; Tapiador, F.J.; Hanel, M. Review of GPM IMERG performance: A global perspective. *Remote Sens. Environ.* **2022**, *268*, 112754. [CrossRef]
36. Lv, P.F.; Hao, H.F.; Wu, G.C. Differences in Global Precipitation Regimes Between Land and Ocean Areas Based on the GPM IMERG Product. *Remote Sens.* **2023**, *15*, 4179. [CrossRef]
37. Jiang, S.H.; Wei, L.Y.; Ren, L.L.; Zhang, L.Q.; Wang, M.H.; Cui, H. Evaluation of IMERG, TMPA, ERA5, and CPC precipitation products over mainland China: Spatiotemporal patterns and extremes. *Water Sci. Eng.* **2023**, *16*, 45–56. [CrossRef]
38. Li, R.Z.; Qi, D.; Zhang, Y.; Wang, K.C. A new pixel-to-object method for evaluating the capability of the GPM IMERG product to quantify precipitation systems. *J. Hydrol.* **2022**, *613*, 128476. [CrossRef]
39. Xu, R.; Tian, F.Q.; Yang, L.; Hu, H.C.; Lu, H.; Hou, A.Z. Ground validation of GPM IMERG and TRMM 3B42V7 rainfall products over southern Tibetan Plateau based on a high-density rain gauge network. *J. Geophys. Res.-Atmos.* **2017**, *122*, 910–924. [CrossRef]
40. He, B.; Huang, L.; Wang, Q. Precipitation deficits increase high diurnal temperature range extremes. *Sci. Rep.* **2015**, *5*, srep12004. [CrossRef]
41. Dai, A. Global precipitation and thunderstorm frequencies. Part II: Diurnal variations. *J. Clim.* **2001**, *14*, 1112–1128. [CrossRef]
42. Li, D.; Qi, Y.; Chen, D. Changes in rain and snow over the Tibetan Plateau based on IMERG and Ground-based observation. *J. Hydrol.* **2022**, *606*, 127400. [CrossRef]
43. Gentilucci, M.; Barbieri, M.; Pambianchi, G. Reliability of the IMERG product through reference rain gauges in Central Italy. *Atmos. Res.* **2022**, *278*, 106340. [CrossRef]
44. Fang, J.; Yang, W.T.; Luan, Y.B.; Du, J.; Lin, A.W.; Zhao, L. Evaluation of the TRMM 3B42 and GPM IMERG products for extreme precipitation analysis over China. *Atmos. Res.* **2019**, *223*, 24–38. [CrossRef]
45. Smith, A.; Lott, N.; Vose, R. The Integrated Surface Database Recent Developments and Partnerships. *Bull. Am. Meteorol. Soc.* **2011**, *92*, 704–708. [CrossRef]
46. Wu, G.; Lv, P.; Mao, Y.; Wang, K. ERA5 Precipitation over China: Better Relative Hourly and Daily Distribution than Absolute Values. *J. Clim.* **2024**, *37*, 1581–1596. [CrossRef]
47. Qin, S.; Wang, K.; Wu, G.; Ma, Z. Variability of hourly precipitation during the warm season over eastern China using gauge observations and ERA5. *Atmos. Res.* **2021**, *264*, 105872. [CrossRef]
48. Wu, G.; Qin, S.; Mao, Y.; Ma, Z.; Shi, C. Validation of Precipitation Events in ERA5 to Gauge Observations during Warm Seasons over Eastern China. *J. Hydrometeorol.* **2022**, *23*, 807–822. [CrossRef]
49. Liu, X.; Ren, Z. Progress in quality control of surface meteorological data. *Meteorol. Sci. Technol.* **2005**, *33*, 199–203. (In Chinese)
50. Ren, Z.; Xiong, A. Operational system development on three-step quality control of observations from AWS. *Meteorol. Mon.* **2007**, *33*, 19–24. (In Chinese)
51. Diamond, H.J.; Karl, T.R.; Palecki, M.A.; Baker, C.B.; Bell, J.E.; Leeper, R.D.; Easterling, D.R.; Lawrimore, J.H.; Meyers, T.P.; Helfert, M.R.; et al. U.S. climate reference network after one decade of operations status and assessment. *Bull. Am. Meteorol. Soc.* **2013**, *94*, 485–498. [CrossRef]
52. Zhang, Y.; Li, R.; Wang, K. Climatology and changes in internal intensity distributions of global precipitation systems over 2001–2020 based on IMERG. *J. Hydrol.* **2023**, *620*, 129386. [CrossRef]

53. Badger, A.M.; Peters-Lidard, C.; Kirschbaum, D.B. A Global Evaluation of IMERG Precipitation Occurrence Using SMAP Detected Soil Moisture Change. *J. Hydrometeorol.* **2022**, *23*, 117–128.
54. Tan, J.; Petersen, W.A.; Tokay, A. A Novel Approach to Identify Sources of Errors in IMERG for GPM Ground Validation. *J. Hydrometeorol.* **2016**, *17*, 2477–2491. [CrossRef]
55. Freitas, E.d.S.; Coelho, V.H.R.; Xuan, Y.Q.; Melo, D.; Gadelha, A.N.; Santos, E.A.; Galvao, C.D.; Ramos, G.M.; Barbosa, L.R.; Huffman, G.J.; et al. The performance of the IMERG satellite-based product in identifying sub-daily rainfall events and their properties. *J. Hydrol.* **2020**, *589*, 125128. [CrossRef]
56. Trenberth, K.E.; Zhang, Y. How Often Does It Really Rain? *Bull. Am. Meteorol. Soc.* **2018**, *99*, 289–298. [CrossRef]
57. Yong, B.; Ren, L.L.; Hong, Y.; Wang, J.H.; Gourley, J.J.; Jiang, S.H. Chen, X.; Wang, W. Hydrologic evaluation of Multisatellite Precipitation Analysis standard precipitation products in basins beyond its inclined latitude band: A case study in Laohahe basin, China. *Water Resour. Res.* **2010**, *46*, 759–768. [CrossRef]
58. Tang, G.Q.; Ma, Y.Z.; Long, D.; Zhong, L.Z.; Hong, Y. Evaluation of GPM Day-1 IMERG and TMPA Version-7 legacy products over Mainland China at multiple spatiotemporal scales. *J. Hydrol.* **2016**, *533*, 152–167. [CrossRef]
59. Prakash, S.; Mitra, A.K.; AghaKouchak, A.; Liu, Z.; Norouzi, H.; Pai, D.S. A preliminary assessment of GPM-based multi-satellite precipitation estimates over a monsoon dominated region. *J. Hydrol.* **2018**, *556*, 865–876. [CrossRef]
60. Ebert, E.E.; Janowiak, J.E.; Kidd, C. Comparison of near-real-time precipitation estimates from satellite observations and numerical models. *Bull. Am. Meteorol. Soc.* **2007**, *88*, 47–64. [CrossRef]
61. Gerapetritis, H.; Pelissier, J.M. The critical success index and warning strategy. In Proceedings of the 17th Conference on Probability and Statistics in Atmospheric Sciences, Seattle, WA, USA, 11–15 January 2004; American Meteorological Society: Seattle, WA, USA, 2004.
62. Warner, M.D.; Mass, C.F.; Salathé, E.P. Wintertime Extreme Precipitation Events along the Pacific Northwest Coast: Climatology and Synoptic Evolution. *Mon. Weather Rev.* **2012**, *140*, 2021–2043. [CrossRef]
63. Lee, S.H.; Polvani, L.M.; Guan, B. Modulation of Atmospheric Rivers by the Arctic Stratospheric Polar Vortex. *Geophys. Res. Lett.* **2022**, *49*, e2022GL100381. [CrossRef]
64. Wang, J.X.; Petersen, W.A.; Wolff, D.B. Validation of Satellite-Based Precipitation Products from TRMM to GPM. *Remote Sens.* **2021**, *13*, 1745. [CrossRef]
65. Han, X.; Xue, H.; Zhao, C.; Lu, D. The roles of convective and stratiform precipitation in the observed precipitation trends in Northwest China during 1961-2000. *Atmos. Res.* **2016**, *169*, 139–146. [CrossRef]
66. He, Z.; Zhang, Q.; Sun, J. The Contribution of Mesoscale Convective Systems to Intense Hourly Precipitation Events During the Warm Seasons over Central East China. *Adv. Atmos. Sci.* **2016**, *33*, 1233–1239. [CrossRef]
67. Derin, Y.; Kirstetter, P.E. Evaluation of IMERG Over CONUS Complex Terrain Using Environmental Variables. *Geophys. Res. Lett.* **2022**, *49*, e2022GL100186. [CrossRef]
68. Zhou, T.; Yu, R.; Chen, H.; Dai, A.; Pan, Y. Summer precipitation frequency, intensity, and diurnal cycle over China: A comparison of satellite data with rain gauge observations. *J. Clim.* **2008**, *21*, 3997–4010. [CrossRef]
69. Ramadhan, R.; Yusnaini, H.; Ningsih, A.P.; Hashiguchi, H.; Shimomai, T.; Vonnisa, M.; Ulfah, S.; Suryanto, W.; Sholihun, S. Ground validation of GPM IMERG-F precipitation products with the point rain gauge records on the extreme rainfall over a mountainous area of Sumatra Island. *J. Penelit. Pendidik. IPA* **2022**, *8*, 163–170. [CrossRef]
70. Kidd, C.; Becker, A.; Huffman, G.J.; Muller, C.L.; Joe, P.; Skofronick-Jackson, G.; Kirschbaum, D.B. So, How Much of the Earth's Surface Is Covered by Rain Gauges? *Bull. Am. Meteorol. Soc.* **2017**, *98*, 69–78. [CrossRef]
71. Cattoen, C.; Robertson, D.E.; Bennett, J.C.; Wang, Q.J.; Carey-Smith, T.K. Calibrating Hourly Precipitation Forecasts with Daily Observations. *J. Hydrometeorol.* **2020**, *21*, 1655–1673. [CrossRef]
72. Zheng, Y.G.; Gong, Y.D.; Chen, J.; Tian, F.Y. Warm-Season Diurnal Variations of Total, Stratiform, Convective, and Extreme Hourly Precipitation over Central and Eastern China. *Adv. Atmos. Sci.* **2019**, *36*, 143–159. [CrossRef]
73. Guerreiro, S.B.; Fowler, H.J.; Barbero, R.; Westra, S.; Lenderink, G.; Blenkinsop, S.; Lewis, E.; Li, X.F. Detection of continental-scale intensification of hourly rainfall extremes. *Nat. Clim. Change* **2018**, *8*, 803–807. [CrossRef]
74. Marelle, L.; Myhre, G.; Hodnebrog, O.; Sillmann, J.; Samset, B.H. The Changing Seasonality of Extreme Daily Precipitation. *Geophys. Res. Lett.* **2018**, *45*, 11352–11360. [CrossRef]
75. Silva, F.D.D.; da Costa, C.P.W.; Franco, V.D.; Gomes, H.B.; da Silva, M.C.L.; Vanderlei, M.H.G.D.; Costa, R.L.; da Rocha, R.L.; Cabral, J.B.; dos Reis, J.S.; et al. Intercomparison of Different Sources of Precipitation Data in the Brazilian Legal Amazon. *Climate* **2023**, *11*, 241. [CrossRef]
76. Merino, A.; Garcia-Ortega, E.; Navarro, A.; Fernandez-Gonzalez, S.; Tapiador, F.J.; Sanchez, J.L. Evaluation of gridded rain-gauge-based precipitation datasets: Impact of station density, spatial resolution, altitude gradient and climate. *Int. J. Climatol.* **2021**, *41*, 3027–3043. [CrossRef]
77. Contractor, S.; Donat, M.G.; Alexander, L.V. Changes in observed daily precipitation over global land areas since 1950. *J. Clim.* **2021**, *34*, 3–19. [CrossRef]

78. Polade, S.D.; Pierce, D.W.; Cayan, D.R.; Gershunov, A.; Dettinger, M.D. The key role of dry days in changing regional climate and precipitation regimes. *Sci. Rep.* **2014**, *4*, 4364. [CrossRef]
79. Fu, Y.Y.; Mao, Y.A.; Wu, G.C. Event-based evaluation of urbanization impact on precipitation during the 1978–2021 warm season over eastern China. *Urban Clim.* **2024**, *56*, 102048. [CrossRef]